A Pipeline for Automated Voxel Dosimetry: Application in Patients with Multi-SPECT/CT Imaging After ^{177}Lu-Peptide Receptor Radionuclide Therapy

Yuni K. Dewaraja[1], David M. Mirando[2], Avery B. Peterson[1,3], Jeremy Niedbala[1], John D. Millet[1], Justin K. Mikell[4], Kirk A. Frey[1], Ka Kit Wong[1], Scott J. Wilderman[1], and Aaron S. Nelson[2]

[1]Department of Radiology, University of Michigan, Ann Arbor, Michigan; [2]MIM Software Inc., Cleveland, Ohio; [3]Department of Radiation Oncology, Wayne State University, Detroit, Michigan; and [4]Radiation Oncology, University of Michigan, Ann Arbor, Michigan

Patient-specific dosimetry in radiopharmaceutical therapy (RPT) is impeded by the lack of tools that are accurate and practical for the clinic. Our aims were to construct and test an integrated voxel-level pipeline that automates key components (organ segmentation, registration, dose-rate estimation, and curve fitting) of the RPT dosimetry process and then to use it to report patient-specific dosimetry in ^{177}Lu-DOTATATE therapy. **Methods:** An integrated workflow that automates the entire dosimetry process, except tumor segmentation, was constructed. First, convolutional neural networks (CNNs) are used to automatically segment organs on the CT portion of one post-therapy SPECT/CT scan. Second, local contour intensity–based SPECT–SPECT alignment results in volume-of-interest propagation to other time points. Third, dose rate is estimated by explicit Monte Carlo (MC) radiation transport using the fast, Dose Planning Method code. Fourth, the optimal function for dose-rate fitting is automatically selected for each voxel. When reporting mean dose, we apply partial-volume correction, and uncertainty is estimated by an empiric approach of perturbing segmentations. **Results:** The workflow was used with 4-time-point ^{177}Lu SPECT/CT imaging data from 20 patients with 77 neuroendocrine tumors, segmented by a radiologist. CNN-defined kidneys resulted in high Dice values (0.91–0.94) and only small differences (2%–5%) in mean dose when compared with manual segmentation. Contour intensity–based registration led to visually enhanced alignment, and the voxel-level fitting had high R^2 values. Across patients, dosimetry results were highly variable; for example, the average of the mean absorbed dose (Gy/GBq) was 3.2 (range, 0.2–10.4) for lesions, 0.49 (range, 0.24–1.02) for left kidney, 0.54 (range, 0.31–1.07) for right kidney, and 0.51 (range, 0.27–1.04) for healthy liver. Patient results further demonstrated the high variability in the number of cycles needed to deliver hypothetical threshold absorbed doses of 23 Gy to kidney and 100 Gy to tumor. The uncertainty in mean dose, attributable to variability in segmentation, averaged 6% (range, 3%–17%) for organs and 10% (range, 3%–37%) for lesions. For a typical patient, the time for the entire process was about 25 min (~2 min manual time) on a desktop computer, including time for CNN organ segmentation, coregistration, MC dosimetry, and voxel curve fitting. **Conclusion:** A pipeline integrating novel tools that are fast and automated provides the capacity for clinical translation of dosimetry-guided RPT.

Key Words: radionuclide therapy; theranostics; SPECT/CT; ^{177}Lu; dosimetry; Monte Carlo

Received Dec. 21, 2021; revision accepted Mar. 23, 2022.

For correspondence or reprints, contact Yuni K. Dewaraja (yuni@umich.edu).

Published online Apr. 14, 2022.

J Nucl Med 2022; 63:1665–1672
DOI: 10.2967/jnumed.121.263738

Radiopharmaceutical therapy (RPT) is well suited to the theranostic treatment approach because imaging after one cycle could be used to predict absorbed doses per unit activity that would be delivered from subsequent cycles. Thus, the injected activity or number of cycles can be modulated on an individualized basis to potentially enhance therapeutic efficacy while keeping organ toxicities at an acceptable level (*1–3*). Despite this potential, fixed-activity protocols continue to be used in RPTs such as ^{177}Lu-DOTATATE peptide receptor radionuclide therapy (PRRT), for which the standard practice is to deliver 4 cycles at 7.4 GBq/cycle (*1*).

In RPT dosimetry, 3-dimensional patient images coupled with voxel-level dose estimation using methods such as Monte Carlo (MC) radiation transport can account for spatial and temporal activity nonuniformity, as well as tissue heterogeneity, down to the resolution limit of the imaging system. This method contrasts with traditional methods that approximate the anatomy by a reference phantom model and provide only the average absorbed dose to structures that may not provide sufficient information to predict potential biologic effects (*4*). However, voxel dosimetry can be logistically difficult to implement because of the need for repeated SPECT imaging with relatively long acquisitions, typically 20–30 min (*5*); coregistration of sequential images and voxel-level curve fitting; and the computational cost of accurate dose-rate estimation using direct MC radiation transport. The potential for reducing the imaging burden associated with dosimetry has recently been reported (*6*). However, there is much room to improve the efficiency and accuracy of the other steps above, as well as volume-of-interest (VOI) segmentation, which is needed to report dose metrics to lesions or organs.

Recent advances in automated medical image segmentation using deep learning methods focus mostly on external-beam radiotherapy applications (*7*). Despite the potential for substantially reducing the variability and labor associated with segmentation, well-validated deep learning tools are not yet routinely available with RPT dosimetry software. Although segmentation in RPT dosimetry is often performed on emission images, segmentation on coregistered morphologic images (CT, MRI) exploits their superior spatial resolution. The non–contrast-enhanced low-dose CT component of integrated SPECT/CT and PET/CT systems is suitable for segmenting some organs and well-defined lesions.

Among voxel dosimetry methods, MC is the consensus reference standard that is superior to simpler methods such as dose voxel (or point) kernel convolution (DVK) in the presence of tissue heterogeneity. However, RPT dosimetry using general-purpose MC codes (e.g., GEANT4 and MCNP) involve long simulation times, typically hours, to achieve reasonable statistics (*8*). The Dose Planning Method (DPM) MC code, optimized specifically for dose computations in voxelated geometries derived from CT scans, was originally developed, benchmarked, and experimentally validated for fast dose estimation in external-beam radiotherapy (*9*). We previously adapted DPM for application in ^{131}I radioimmunotherapy by sampling decay locations internally within the voxelated geometry and benchmarked it (*10*). Recently, we performed measurements with radiochromic film to directly validate DPM for ^{177}Lu and ^{131}I (*11*). As detailed in Sempau et al. (*9*), DPM achieves its computational efficiency while maintaining accuracy using simplified cross-sectional models that are accurate at energies relevant to radiation therapy and by using the delta scattering technique for photon transport and the random hinge transport mechanics model for electron transport, which permits long transport steps across voxel boundaries.

Our aim was to construct and test a voxel-dosimetry pipeline that integrates deep learning–based segmentation, fast MC dose estimation, and other automated processes and to use it to report highly patient-specific dosimetry using multi-SPECT/CT imaging after ^{177}Lu-PRRT.

MATERIALS AND METHODS

Dosimetry Pipeline

The dosimetry pipeline (Fig. 1) combining automated tools was implemented as a workflow within a commercial software platform (MIM Software Inc.). The only parts of the process that are not integrated are lesion segmentation and partial-volume correction (PVC), which is applied as a postprocessing step when reporting mean absorbed dose only. The workflow is currently in a beta testing stage. Following regulatory review and licensing agreements between the University of Michigan and MIM Software, an MC-based dosimetry workflow as described in this work will be made available for clinical use via MIM.

Segmentation. Organ segmentation was performed on the CT portion of the SPECT/CT scan at the reference time point, which is the time point at which the CT was performed at a higher x-ray tube current and exposure (mAs) than at the other time points. For kidney and liver, we constructed convolutional neural networks (CNNs) based on RefineNet (*12*), which is based on the U-Net architecture with 3-dimensional convolution blocks to better leverage contextual information from all directions. The CNNs for kidney and liver were trained with 65 and 108 manually contoured datasets, respectively, with 5-fold cross validation. The previously evaluated Dice scores from these tests averaged 0.93 ± 0.04 and 0.97 ± 0.05 for the kidneys (*13*) and liver (*14*), respectively. In the current study, we tested the CNN for liver by visual assessment and for kidney by calculating geometric similarity measures (Dice and mean distance to agreement [MDA]) and comparing dose estimates relative to manual segmentations performed by an experienced technologist and checked by a radiologist. Dice is a spatial overlap index, and MDA is a spatial distance–based metric; both are widely used to assess the reliability of segmentations.

Automatic segmentation of lesions such as neuroendocrine tumor (NET) is not yet sufficiently developed and validated. Therefore, lesions (≤5) were manually segmented by a radiologist on the patient's diagnostic-quality baseline CT or MRI scan and then transferred to the reference SPECT/CT scan after coregistration. If misregistration was evident, the location was manually adjusted on the basis of SPECT uptake. Lesions clearly visible on the CT portion of the reference SPECT/CT scan were directly defined there. Only lesions that were well defined and more than 2 cm^3 in volume were segmented, to avoid large uncertainties. The healthy liver was defined as the liver minus any segmented lesions and therefore included any unsegmented lesions.

Local Contour Intensity–Guided Registration. To coregister sequential images, contour intensity–based SPECT–SPECT alignment was used. SPECT images are first rigidly registered to the reference SPECT images as a gross alignment. The SPECT intensity information on voxels within each selected VOI plus a surrounding 7-cm expansion zone is then used to perform multiple local rigid registrations between the images. These locally focused alignments are rigidly spliced together to generate a composite image aligned and interpolated to the grid of the reference SPECT images. In this process, VOIs are automatically propagated from the reference to other time points. We tested this automated method previously in a subset of patients by comparing time-integrated activity values relative to rigidly transferred VOIs with visual fine tuning and reported good agreement: 0.3% (95% CI, −8.0% to 8.7%) for kidneys and 1.9% (95% CI, −17.8% to 21.7%) for tumors (*15*).

Voxel Dose-Rate Estimation. Details on the MC transport mechanics and physics data based on PENELOPE can be found in the original paper on DPM development (*9*) and our subsequent paper (*10*) on extension to RPT. For the current work, the ^{177}Lu decay and spectral information came from NuDat 3.0 (*16*) and BetaShape 2.2 (*17*). The cutoffs for photon and electron transport were set to 4 keV and 59 keV, respectively, below which energy was locally deposited in the voxel. These cutoffs are reasonable, considering that the range of a 59-keV electron in tissue (~0.07 mm) and the mean free path of a 4-keV photon in tissue (~0.1 mm) are much smaller than the voxel size of the dose-rate map. For a typical case (patient 12), we tested this assumption by running DPM with lower cutoffs (photons, 2 keV;

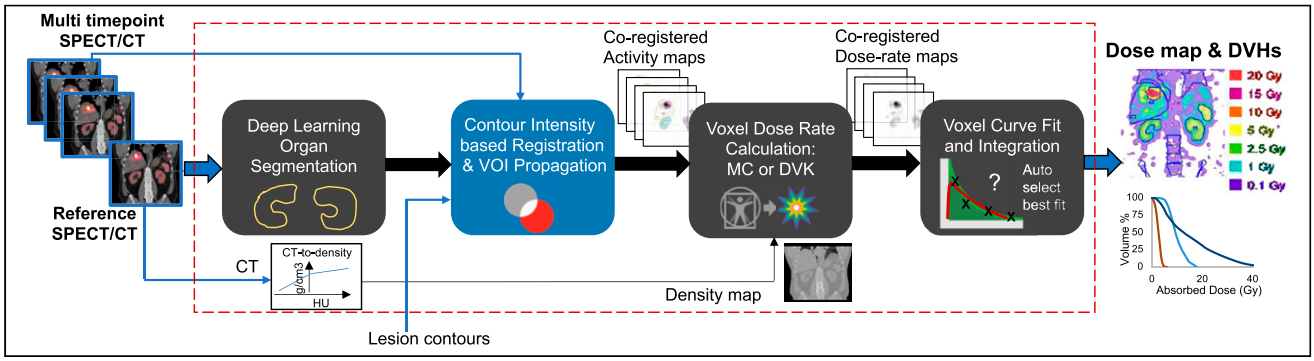

FIGURE 1. Overview of automated dosimetry workflow. At reference time point, CT of SPECT/CT was performed at higher mAs value than at other time points. HU = Hounsfield units.

electrons, 20 keV), which results in a 20% increase in run time, but the average difference in voxel dose rate in a VOI was only 0.5%.

Dose-rate estimation by DPM MC and DVK convolution with soft-tissue kernels precalculated using DPM were integrated as options within the dosimetry workflow to enable comparison. Exploiting the high speed of Fast Fourier Transform convolution, we chose to work with a large kernel (267 × 267 × 267 [3 mm × 3 mm × 3 mm]) to ensure capturing of photon dose contribution from decays anywhere within the SPECT field of view. The mass density map for MC transport or for density scaling of the DVK results is generated via a CT-to-density calibration curve, which we determined specifically for our system. The coregistered quantitative SPECT image and the reference time-point density map are the inputs to the dose-rate calculation, which is repeated at each time point. Images are resampled to 167 × 167 × 131 (3 mm × 3 mm × 3 mm) for DVK and to 128 × 128 × 100 (3.91 mm × 3.91 mm × 3.91 mm) for MC. After testing statistical uncertainty, 10^8 histories were selected for the MC simulations.

Voxel-Level Curve Fitting to Generate Dose Maps. At each voxel, dose-rate $\dot{D}$ as a function of time is fit by a monoexponential and a 3-parameter (C1, λ_1, λ_2) biexponential of the form $\dot{D}(t) = C_1(e^{-\lambda_1 t} - e^{-\lambda_2 t})$ using standard least-squares optimization. Next, the best fit function is automatically selected independently for each voxel on the basis of the Akaike information criterion as proposed by Sarrut et al. (*18*). Other options such as trapezoidal approximation as well as a 4-parameter biexponential, suitable when more time points are available, were implemented but not used in the current study. Dose-rate functions are integrated analytically to generate the dose map.

Mean Absorbed Dose and Dose–Volume Histogram (DVH) Metrics. The segmented contours are applied to the absorbed dose map to generate the mean absorbed dose and other DVH metrics. Absorbed dose estimates derived from SPECT images are degraded by partial-volume errors associated with limited spatial resolution. For mean value PVC, we determined recovery coefficients (RCs), defined as the ratio of SPECT-measured activity to true activity (*19*) within CT-defined sphere VOIs of a multisphere phantom with sphere-to-background ratio of 6.2:1 and sphere sizes of 2–113 mL. The same SPECT/CT system and imaging and reconstruction parameters as used in the patient studies were used for this phantom experiment. The fit to our RC-versus-volume data was as follows: $RC = 1 - 1/[1 + (v/3.673)^{0.948}]$, where v is the volume in milliliters. This function was used to determine volume-dependent RCs for lesions or organs and were applied (scaling by 1/RC) when reporting mean absorbed doses only.

Patient Characteristics and SPECT/CT Imaging

Patient Studies. Data correspond to 20 patients (Supplemental Table 1; supplemental materials are available at http://jnm.snmjournals.org) with NETs who completed 4-time-point SPECT/CT imaging after cycle 1 of standard ^{177}Lu-DOTATATE PRRT at the University of Michigan Medical Center between August 2018 and July 2021. The research imaging was approved by the Institutional Review Board, and all patients provided written informed consent.

Quantitative SPECT/CT. The SPECT/CT system was a Siemens Intevo Bold equipped with a medium-energy collimator and a 15-mm crystal. The 4 SPECT acquisitions (25 s/view) were performed on days 0 (directly after completion of amino acid infusion), 1, 4–5, and 5–8. Manufacturer-recommended settings of a 20% acquisition window at 208 keV with adjacent 10% scatter windows, a 256 × 256 matrix, and 120 views were used. Siemens xSPECT Quant software was used to directly generate reconstructed images in Bq/mL units. This system requires that a National Institute of Standards and Technology–traceable ^{75}Se calibration source with a 3% uncertainty be used to perform a monthly site-specific check of the system sensitivity and associated fine tuning (*19*). The SPECT reconstruction parameters were 48 iterations (1 subset) of ordered-subset conjugate gradient with resolution recovery, a 256 × 256 × 199 matrix (1.953 mm^3), and no postfiltering (*19*). The non–contrast-enhanced, free-breathing CT was performed at 120 kVp and 80 mAs at the reference time point and at 15 mAs at other time points. The CT reconstruction matrix was 512 × 512 × 130 (0.97 mm × 0.97 mm × 3 mm).

Uncertainty Analysis

In RPT dosimetry, the traditional approach of propagating uncertainties associated with each step has identified VOI delineation as the largest source of variability (*20*). The analytic approach proposed for estimating this variability is not well suited when anatomic imaging is used for segmentation because factors other than spatial resolution (e.g., impact of contrast agents or misalignment with SPECT) can dominate. In addition, the spatial distribution of absorbed dose impacts the uncertainty estimate. Hence, we take an empiric approach of introducing realistic variabilities to the segmented VOIs and determining the corresponding variability in the mean absorbed dose when the perturbed contours are applied to the dose map and the perturbed volumes used to determine RCs. We introduced volume expansions and contractions (organs, ±5% and ±10%; lesions, ±10% and ±20%) and 26 translations of 4 mm (~SPECT voxel size) for each perturbation. These levels were selected on the basis of an ongoing interoperator variability study on lesion segmentation at our institution and on the kidney volume differences for CNN versus manual segmentation in the current study. For each VOI, the relative standard deviation (coefficient of variation [COV]) in mean absorbed dose from all perturbations is reported as the uncertainty.

RESULTS

The results correspond to imaging data after cycle 1, with 18 of 20 patients treated with the 7.4-GBq administration and 2 treated with a reduced level of about 3.2 GBq (Supplemental Table 1). All images associated with patient 6 are shared at University of Michigan Deep Blue data repository: https://doi.org/10.7302/0n8e-rz46 and https://doi.org/10.7302/vhrh-qg23.

Segmentation

Example segmentations are shown in Figure 2. The median lesion volume was 22 (range, 2 − 1,039) mL, and 64 of 77 were in the liver (Supplemental Table 1). In most cases, the CNN organ segmentation was accepted by the radiologist. When manual adjustment was needed, it took only 0.5–3 min per organ. The fine tuning related mostly to inclusion of bowel loops with liver and cysts with kidney (Fig. 2B). Comparing manual versus CNN-defined kidney, Dice scores averaged 0.91 (range, 0.77–0.94) without manual adjustment and 0.93 (range, 0.91–0.94) with manual adjustment, and differences in mean absorbed doses were 3% (range, 0%–21%) without adjustment and 2% (range, 0%–4%) with adjustment (Supplemental Table 2).

Contour Intensity–Based SPECT–SPECT Alignment

Visual inspection showed well-aligned images (Fig. 3) across all time points, with only 3 of 164 VOIs needing manual adjustment. These 3 cases were 2 small lymph node lesions in the pelvis and a lesion in the mesentery when there was substantial movement between scans.

Voxel-Level Curve Fitting

For a typical patient, a map of the coefficient of determination (R^2) that measures the goodness of the fit at each voxel and example dose-rate curve fits are shown in Figure 4. The R^2 values across all voxels in all patients are summarized in Figure 4B. Summary statistics for the effective half-life (T_{eff}) values of the main component of the exponential are presented in Supplemental Table 3.

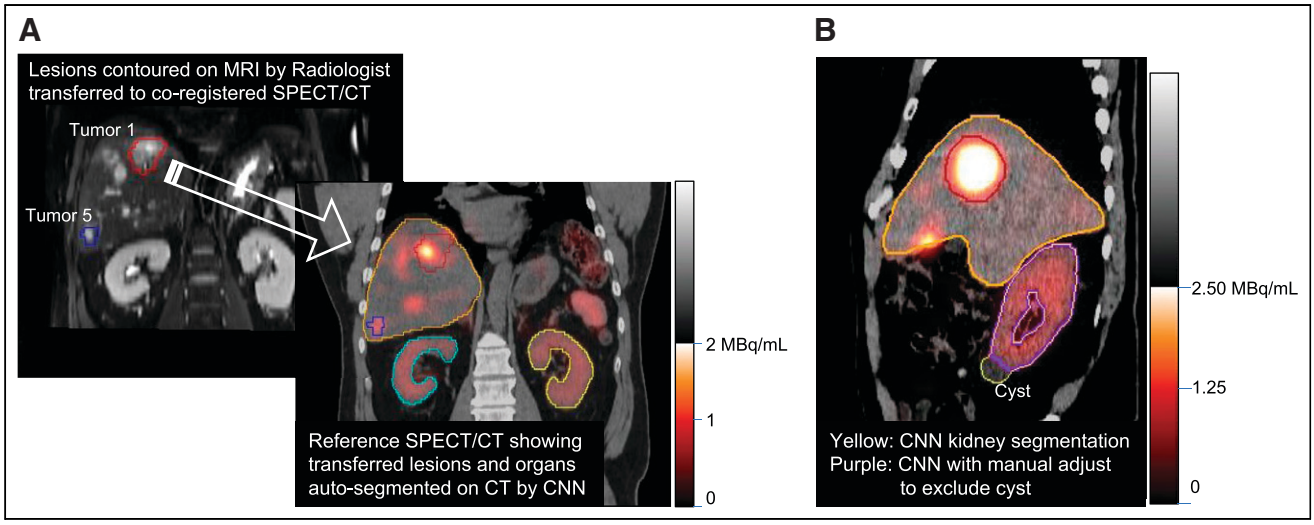

FIGURE 2. Example segmentations for patients 12 (A) and 4 (B). In A, CNN-defined kidney and liver were accepted by radiologist, whereas in B, the CNN-defined kidney (yellow contour) was manually adjusted (purple contour) to avoid a cyst.

Dosimetry

Example MC dose maps and DVHs are presented in Figure 5A. Individual mean absorbed dose values after PVC are presented in Figure 6 and Supplemental Figure 1, and summary statistics averaged across all patients are presented in Supplemental Table 3. The median RCs applied were 0.85 (range, 0.37–1.00) for lesions, 0.97 (range, 0.95–0.98) for kidney, and 1.00 (range, 1.00–1.00) for healthy liver. There was a weak correlation between tumor volume and mean absorbed dose ($R^2 = 0.052$; $P = 0.046$). DVH metrics are presented in Supplemental Figure 2.

Uncertainty in Mean Absorbed Dose Estimates

With 10^8 MC histories, the contribution of statistical uncertainty is negligible. For example, the COV in VOI dose rates (available from the DPM uncertainty maps) was less than 0.2% for the case shown in Figure 5A. The uncertainty associated with SPECT–SPECT misalignment can be approximated empirically by intentionally misaligning the 4 dose-rate maps and repeating the voxel-level automatic fitting process. This process is not practical to perform because of the various combinations of shifts, and we therefore limit this process to 1 illustrative example. This case was chosen because the right kidney is very near a tumor (Fig. 5B), and therefore, the impact of misalignment can be expected to be higher than typical, whereas the other structures are representative of typical patients. With shifts of ±4 mm in all directions, the estimated COV in mean absorbed dose due to misregistration was 1.8%–2.6% for tumor, 1.6% for left kidney, 9.8% for right kidney, and 1.4% for healthy liver. In general, the 4-mm misalignment has a relatively low impact because of the poor resolution of SPECT.

The uncertainty that we report for mean absorbed doses is that associated with segmentation, which also impacts the volume-dependent RCs. The COV, represented as error bars in Supplemental Figure 1, averaged 5% (range, 4%–6%) for left kidney, 7% (range, 3%–17%) for right kidney, 5% (range, 4%–9%) for spleen, 8% (range, 3%–15%) for tumors larger than 10 cm^3, and 16% (range, 8%–37%) for tumors smaller than 10 cm^3. For organs and large tumors, the major contributor to this uncertainty was the contour variability itself, whereas for small tumors it was the sensitivity of RCs to tumor

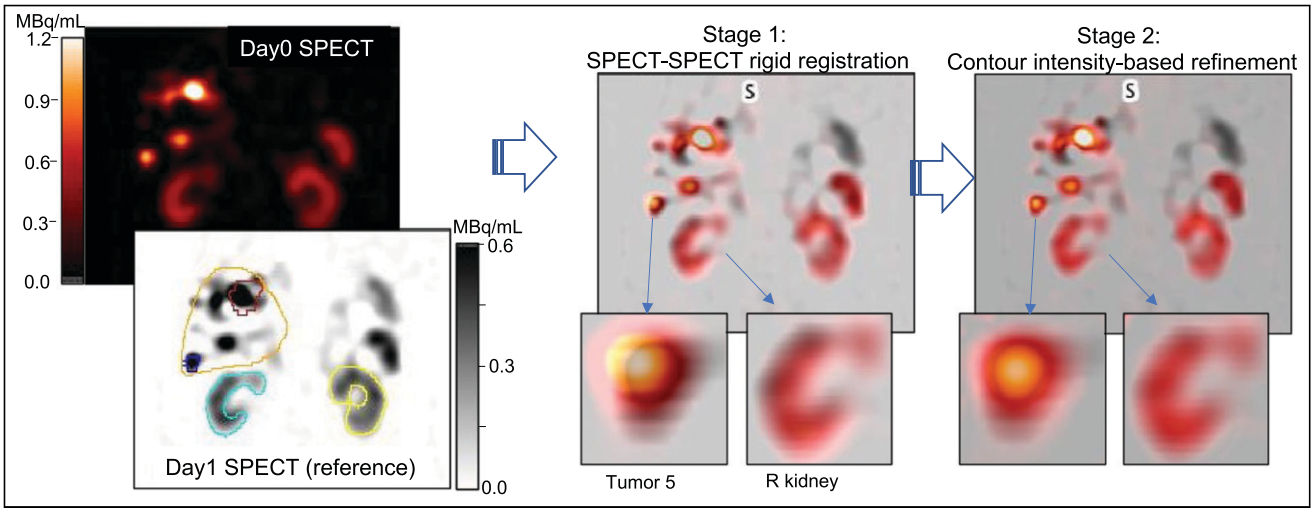

FIGURE 3. Two stages of automatic SPECT–SPECT registration demonstrated for day 0 and day 1 images of patient 12. Comparison of magnified inserts shows subtle improvement in alignment with contour intensity–based refinement.

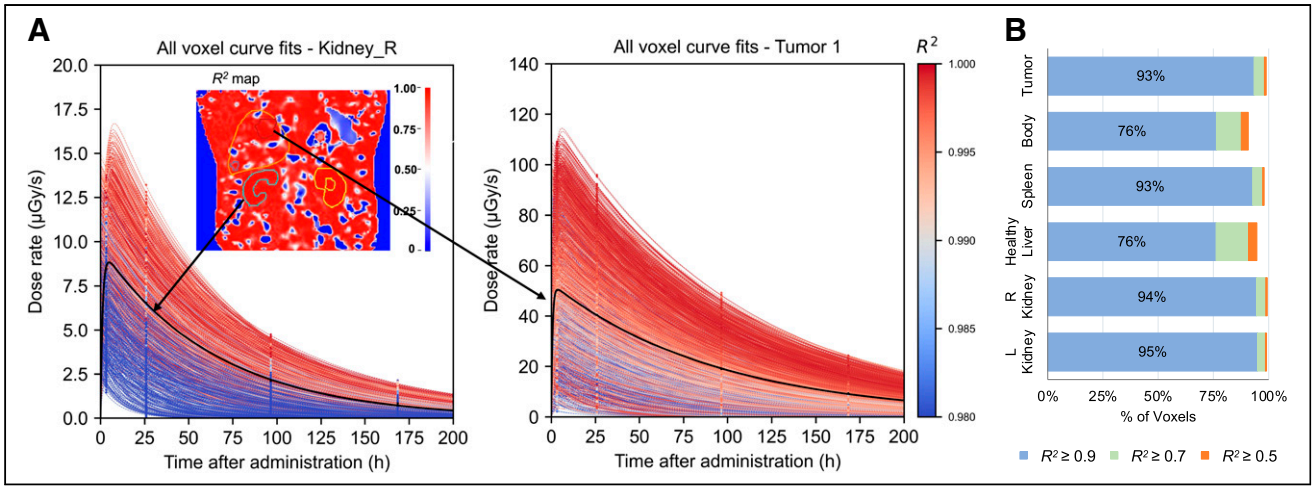

FIGURE 4. (A) Example dose-rate curve fittings for all voxels in right kidney and tumor 1 of patient 12, color-coded by R^2 value of fit. Mono- and biexponential functions are selected for different voxels. Organ-level curve fitting is shown in black. Coronal slice of R^2 map is shown in insert. (B) Percentage of voxels achieving $R^2 > 0.5$, 0.7, and 0.9 for fits across all patients.

volume uncertainty. For example, for tumor volumes smaller than 10 cm^3, the COV in reported absorbed doses increased by a factor of 2 on average when applying RCs, whereas for tumors larger than 100 cm^3 this factor was only 1.1 on average.

Comparison of MC, DVK, and OLINDA

Mean absorbed doses from MC, DVK, and OLINDA 1.0 are compared in Figures 6D and 6E and demonstrate good agreement. For the OLINDA calculation, the organ-level time-integrated activity values from the workflow were used. The difference between DVH metrics from MC and DVK are presented in Supplemental Figure 2.

Computational Cost

All processing was performed on a multicore Mac Pro (3.2 GHz) desktop computer. For a typical patient (128 × 128 × 100 matrix), the total run time starting with 4 SPECT/CT images is about 25 min for the MC option and about 12 min for DVK, of which only about 2 min is manual time. This includes CNN organ segmentation (~2 min), contour-based SPECT alignment (3 min), MC dose-rate estimation (4 min per time point), and voxel-level dose-rate fitting and integration (3 min). DPM currently runs on a single processor but can be accelerated with parallelization.

DISCUSSION

A highly automated pipeline for all steps of RPT voxel dosimetry that needs minimal user interaction was constructed and tested for the ^{177}Lu PRRT application. The automated tools are suitable for other radionuclides and therapies with appropriate testing.

Although activity quantification was not evaluated in the current study, accuracy within 1.2% for large objects has been reported (*19*) with xSPECT Quant software using the same standardized calibration process and reconstruction parameters as used in the current study. Furthermore, the sphere phantom–based RCs reported in that study and in our study are in good agreement. This simplistic PVC has limitations because RCs depend on factors other than the volume of the object, such as shape and activity distribution. For a 2-compartment kidney model with uniform activity in the renal cortex, it has been shown that the RC for the cortex is substantially lower than that for a sphere of equal volume (*21*). Generating geometry- or distribution-specific RCs is beyond the scope of the current study and may not be practical because of wide patient-to-patient

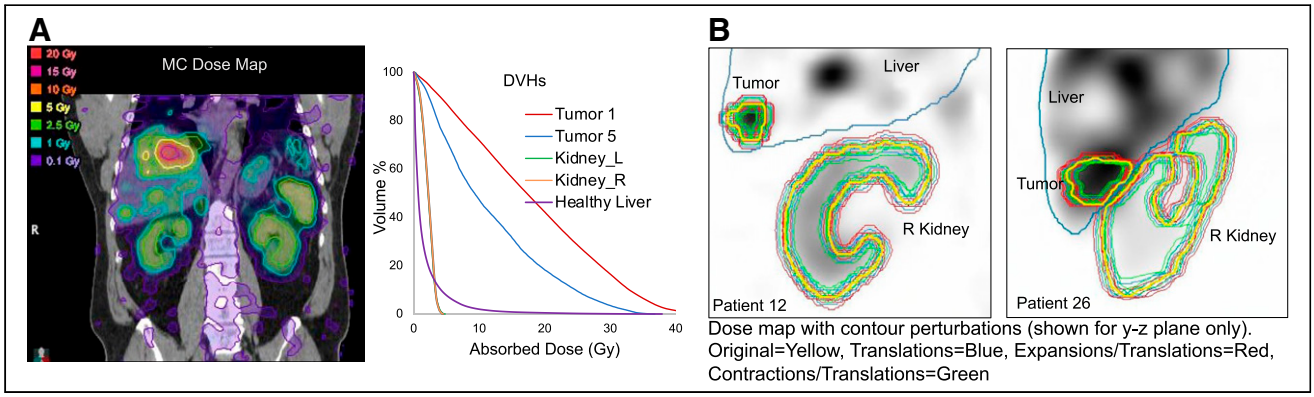

FIGURE 5. (A) Coronal slice of MC dose map and dose–volume histograms for patient 12. (B) Examples of contour perturbations applied to dose maps of patients 12 and 26 for estimating uncertainty. COV in right kidney absorbed dose was 4% for patient 12 but 17% for patient 26 because of proximity to tumor and liver.

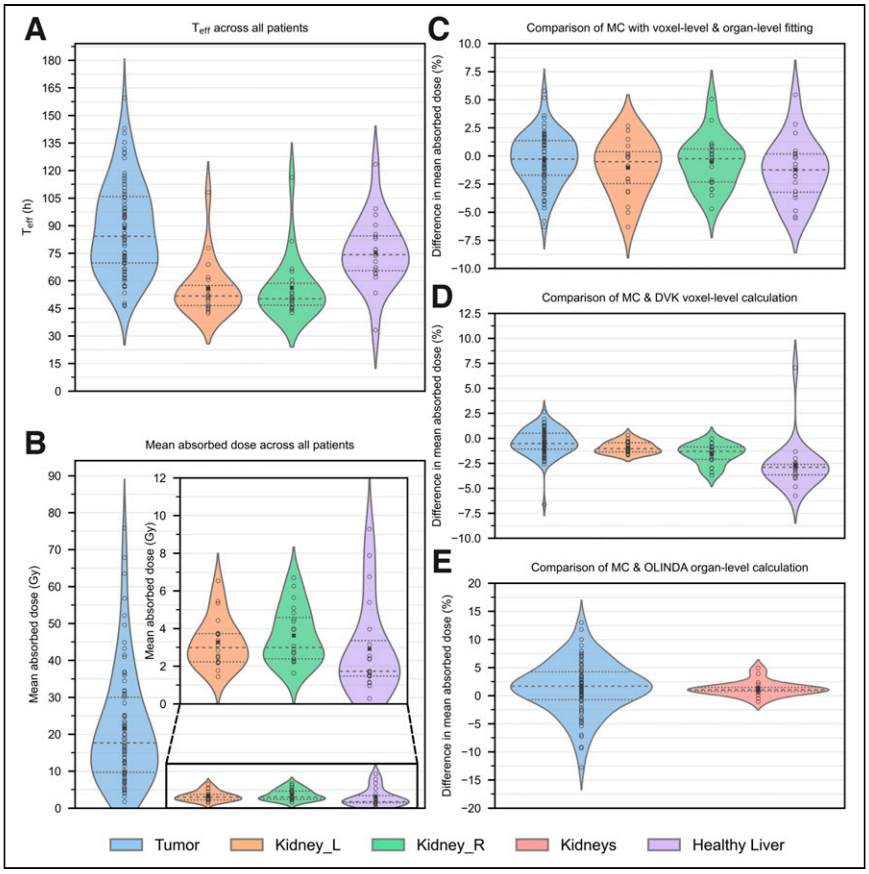

FIGURE 6. Violin plots of dosimetry results across all patients. (A) T_{eff}. (B) Mean absorbed dose with voxel-level MC calculation. (C) Difference in MC dose estimates with voxel-level vs. organ-level dose-rate fitting. (D) Difference between MC and DVK (with density scaling). (E) Difference between MC and OLINDA (with mass scaling). Difference = 100 × (MC − XX)/MC, where XX indicates the other method. Circles indicate individual points, "x" indicates the average across patients, and dashed lines indicate 25th and 75th percentiles.

variations. Despite the limitations, the sphere-based RCs used in our study are widely applied as a mean value correction to mitigate resolution effects in SPECT and PET quantification, including in dosimetry applications (*22,23*).

Ideally, when 3-dimensional dose distributions are being evaluated, PVC should be applied at the voxel level, but this is a challenging and yet-unresolved problem (*24*). Another challenge with voxel dosimetry is that iterative reconstruction with resolution modeling leads to edge artifacts that, depending on the size of the object, can manifest as a visible dip or an overshoot at the center (*25*). This effect and partial-volume effects lead to differences between DVHs derived from SPECT images and those corresponding to the true activity distribution within an object (*26*). Despite the challenges, capturing nonuniformities in the underlying dose distribution to the extent possible is desired when considering biologic effect. There are alternative efforts using deep learning, including by our group (*27*), to mitigate the impact of poor spatial resolution and reconstruction artifacts on voxel dosimetry.

There was close agreement between dose estimates corresponding to manual versus CNN-defined kidney, as is consistent with the findings for a ^{177}Lu-PSMA therapy cohort (*28*). We achieved further improvement with quick manual adjustment of the CNN segmentations. The Dice similarity metrics we achieved are comparable to what is reported for inter- and intraoperator variability in manual organ segmentation (*29*). A possible refinement is to train the CNN to use both CT and SPECT information, which may be beneficial to identify cysts included in kidney contours (Fig. 2B) and to reduce the effects of misregistration between CT and SPECT images (*30*). Visually, the local contour intensity–based SPECT–SPECT registration led to improved alignments compared with global rigid registration (Fig. 3). The main advantage of SPECT intensity–based registration over using CT-based registration to align serial SPECT images is that the former does not depend on SPECT/CT alignment, which is inconsistent because of respiratory motion and patient movement. The automated approach to selecting the optimal fit function led to high R^2 values and is especially beneficial for voxel-level fitting when selection by visual inspection is not feasible. The smooth voxel dose-rate–versus–time data, high R^2 values, and good agreement in T_{eff} when comparing average values from voxel-level versus organ-level fitting give us confidence in the ability to perform accurate voxel-level fitting.

It is notable that the difference between the mean absorbed dose from the OLINDA sphere model and MC was less than 10% for 73 of 77 lesions (Fig. 6E). This difference can, however, be larger for radionuclides with more significant photon yields than ^{177}Lu. The main advantage of MC over conventional DVK methods is in regions of heterogeneous tissue and at steep activity gradients, which are not fully resolved by simple density scaling. Recently, more sophisticated approaches that use multiple kernels to cover media of varying density have been proposed

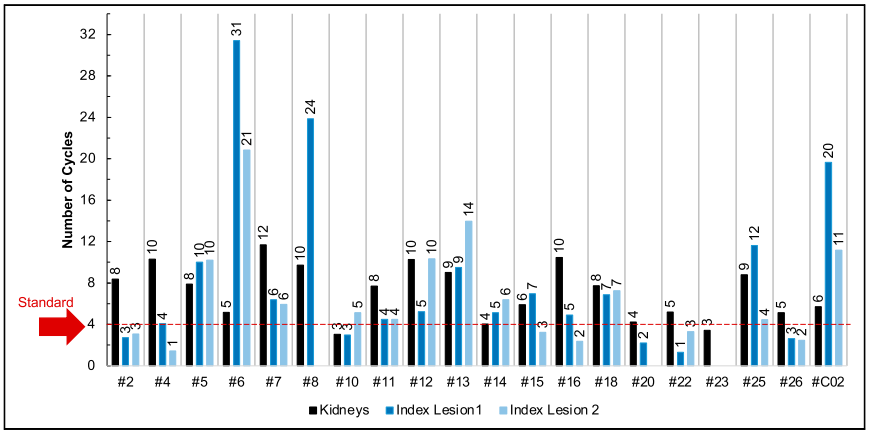

FIGURE 7. Variation in number of 7.4-GBq cycles needed to deliver 23 Gy to kidney and 100 Gy to tumor.

to mitigate the limitations of using a single kernel (*31*). In the current study, lesions in heterogeneous tissue such as bone metastases were not considered because of their small size or the difficulty in defining them. Accurate dosimetry of bone lesions and marrow requires modeling the fine structure of the spongiosa that can be coupled with MC transport (*32*).

RPT dosimetry is typically reported without uncertainty estimates because of the complexity and limitations of traditional error propagation. Although we did not attempt to assess all components of the uncertainty, we captured the main components: the variability associated with contour delineation and the volume-based RCs (*20*). Facilitated by voxel dose maps, our empiric approach of introducing perturbations is both practical to implement and sensitive to each patient's underlying dose distribution, which is not the case with analytic approaches. For example, in patient 26 the relative uncertainty for the right kidney was higher than for the left because of proximity to a lesion in the liver (Fig. 5B); this issue may also explain the higher values reported overall for right versus left in our study and by others (*1,3*).

Across patients, the median T_{eff} that we observed for left (51.7 h) and right (50.3 h) kidney agree closely with previous reports (*1,6*) for similar cohorts. The median absorbed dose to the left (0.41 Gy/GBq) and right (0.43 Gy/GBq) kidneys can be compared with past reported values of 0.61 (*1*), 0.54 (*2*), 0.47 (*33*), and 0.38 (average) (*34*) Gy/GBq for the kidneys. Differences can be attributed to differences in patient cohorts, quantification or dosimetry methods, and renoprotective amino acid preparation. The median value of the mean absorbed dose to tumor in our study (17.7 Gy or 2.7 Gy/GBq) is lower than the per-cycle median values of 50 Gy (*23*) and 4.4 Gy/GBq (*2*) reported for 2 other studies. This difference is not surprising because instead of the anatomic lesion segmentation used in our study, SPECT thresholding was used in the first study whereas the second used VOIs placed over the area of maximum uptake.

Although we do not report biologic effective dose, it can be calculated using the dose-rate maps and fit parameters available from the workflow coupled with published values for the radiobiologic parameters as outlined by Baechler et al. (*35*). Furthermore, since most patients in our study had not yet finished their 4-cycle treatment, no attempt was made to evaluate dose–outcome relationships. PRRT clinical trials in which dosimetry is used solely to avoid toxicity to critical organs have been reported (*1–3*). Performing both tumor and organ dosimetry enables consideration of both efficacy and toxicity when planning subsequent cycles. As a hypothetical example, using the cycle 1 mean dose estimates from our study, we determined the number of cycles each patient would need to receive 100 Gy to tumor and 23 Gy to kidney assuming the same number of grays per cycle. These thresholds, though somewhat arbitrary, were selected here on the basis of a dose–response finding for NETs (*23*) and the generally accepted 23-Gy limit for nephrotoxicity in external-beam radiotherapy, although this limit is likely too low for PRRT. Most patients could receive more than the standard 4 cycles without exceeding 23 Gy to kidney, and most lesions need more than 4 cycles to achieve 100 Gy to tumor (Fig. 7). Access to this type of information in real time via efficient dosimetry calculations will enable clinicians to make well-informed treatment decisions. Furthermore, highly patient-specific dosimetry results are needed to establish the validity of simplified protocols.

CONCLUSION

Multiple steps of the dosimetry chain, organ segmentation, coregistration, dose-rate estimation by MC, and curve fitting were automated and integrated to construct an efficient pipeline for voxel dosimetry that was tested using imaging data from ^{177}Lu-PRRT patients. Facilitated by this efficient workflow, highly patient-specific dosimetry results, including uncertainty estimates, were reported. The speed, automation, and accuracy that were achieved will facilitate implementation of real-time dosimetry-guided RPT in the clinical setting.

DISCLOSURE

This work was supported by grant R01CA240706, an Academic–Industry Partnership award from the National Cancer Institute. Yuni Dewaraja is a consultant for MIM Software, and David Mirando and Aaron Nelson are employees of MIM. No other potential conflict of interest relevant to this article was reported.

KEY POINTS

QUESTION: Can accurate and highly patient-specific dosimetry be performed in a clinical setting to guide RPT?

PERTINENT FINDINGS: An automated pipeline that includes CNNs for organ segmentation and a fast MC code for dose estimation was constructed, tested, and applied to report dosimetry in patients undergoing ^{177}Lu-PRRT. Excluding the time for lesion segmentation, voxel-level MC dose estimates were achieved in about 25 min.

IMPLICATIONS FOR PATIENT CARE: Patient-specific real-time dosimetry, such as performed in the current study after cycle 1, can be used to tailor subsequent cycles on the basis of efficacy and toxicity considerations.

REFERENCES

1. Sundlöv A, Sjögreen-Gleisner K, Svensson J, et al. Individualised ^{177}Lu-DOTATATE treatment of neuroendocrine tumours based on kidney dosimetry. *Eur J Nucl Med Mol Imaging.* 2017;44:1480–1489.
2. Del Prete M, Buteau, FA, Arsenault F, et al. Personalized ^{177}Lu-octreotate peptide receptor radionuclide therapy of neuroendocrine tumours: initial results from the P-PRRT trial. *Eur J Nucl Med Mol Imaging.* 2019;46:728–742.
3. Sandström M, Garske-Roman U, Johansson S, et al. Kidney dosimetry during ^{177}Lu-DOTATATE therapy in patients with neuroendocrine tumors: aspects on calculation and tolerance. *Acta Oncol.* 2018;57:516–521.
4. O'Donoghue JA. Implications of nonuniform tumor doses for radioimmunotherapy. *J Nucl Med.* 1999;40:1337–1341.
5. Rydén T, Van Essen M, Marin I, Svensson J, Bernhardt P. Deep-learning generation of synthetic intermediate projections improves ^{177}Lu SPECT images reconstructed with sparsely acquired projections. *J Nucl Med.* 2021;62:528–535.
6. Hänscheid H, Lapa C, Buck AK, Lassmann M, Werner RA. Dose mapping after endoradiotherapy with ^{177}Lu-DOTATATE/DOTATOC by a single measurement after 4 days. *J Nucl Med.* 2018;59:75–81.
7. Sahiner B, Pezeshk A, Hadjiiski LM, et al. Deep learning in medical imaging and radiation therapy. *Med Phys.* 2019;46:e1–e36.
8. Huizing DMV, de Wit-van der Veen BJ, Verheij M, Stokkel MPM. Dosimetry methods and clinical applications in peptide receptor radionuclide therapy for neuroendocrine tumours: a literature review. *EJNMMI Res.* 2018;8:89. 9.
9. Sempau J, Wilderman SJ, Bielajew AF. DPM, a fast, accurate Monte Carlo code optimized for photon and electron radiotherapy treatment planning dose calculations. *Phys Med Biol.* 2000;45:2263–2291.
10. Wilderman SJ, Dewaraja YK. Method for fast CT/SPECT-based 3D Monte Carlo absorbed dose computations in internal emitter therapy. *IEEE Trans Nucl Sci.* 2007;54:146–151.
11. Van B, Dewaraja YK, Niedbala J, et al. Reproducible absorbed dose measurements for validating dosimetry of short range therapeutic unsealed beta sources including Monte Carlo-based calculations [abstract]. *J Nucl Med.* 2021;62(suppl 1):1577.

12. Lin G, Milan A, Shen C, Reid I. RefineNet: multi-path refinement networks for high-resolution semantic segmentation. https://arxiv.org/abs/1611.06612. Published November 20, 2016. Revised November 25, 2016. Accessed July 13, 2022.
13. Cole N, Wan H, Niedbala J, et al. Impact of a 3D convolution neural network method on liver segmentation: an accuracy and time-savings evaluation. AAPM website. https://w3.aapm.org/meetings/2020AM/programInfo/programAbs.php?sid=8489&aid=51984. Accessed July 13, 2022.
14. Lamba N, Wan H, Kruzer A, et al. Clinical utility of a 3D convolutional neural network kidney segmentation method for radionuclide dosimetry [abstract]. *J Nucl Med.* 2019;60(suppl 1):267.
15. Mirando D, Dewaraja YK, Cole N, Nelson AS. In pursuit of fully automated dosimetry: evaluation of an automatic VOI propagation algorithm using contour intensity-based SPECT alignments. *Eur J Nucl Med Mol Imaging.* 2020;47(suppl 1):S236.
16. NuDat 3.0. National Nuclear Data Center website. https://www.nndc.bnl.gov/nudat3/. Accessed July 13, 2022.
17. Software and tools developed by the LNHB. Laboratorie National Henri Becquerel website. http://www.lnhb.fr/rd-activities/spectrum-processing-software/. Accessed July 13, 2022.
18. Sarrut D, Halty A, Badel JN, Ferrer L, Bardiès M. Voxel-based multimodel fitting method for modeling time activity curves in SPECT images. *Med Phys.* 2017;44:6280–6288.
19. Tran-Gia J, Lassmann M. Characterization of noise and resolution for quantitative ^{177}Lu SPECT/CT with xSPECT Quant. *J Nucl Med.* 2019;60:50–59.
20. Gear JI, Cox MG, Gustafsson J, et al. EANM practical guidance on uncertainty analysis for molecular radiotherapy absorbed dose calculations. *Eur J Nucl Med Mol Imaging.* 2018;45:2456–2474.
21. Tran-Gia J, Lassmann M. Optimizing image quantification for ^{177}Lu SPECT/CT based on a 3D printed 2-compartment kidney phantom. *J Nucl Med.* 2018;59:616–624.
22. Finocchiaro D, Berenato S, Grassi E, et al. Partial volume effect of SPECT images in PRRT with ^{177}Lu labelled somatostatin analogues: a practical solution. *Phys Med.* 2019;57:153–159.
23. Ilan E, Sandström M, Wassberg C, et al. Dose response of pancreatic neuroendocrine tumors treated with peptide receptor radionuclide therapy using ^{177}Lu-DOTATATE. *J Nucl Med.* 2015;56:177–182.
24. Tran-Gia J, Salas-Ramirez M, Lassmann M. What you see is not what you get: on the accuracy of voxel-based dosimetry in molecular radiotherapy. *J Nucl Med.* 2020;61:1178–1186.
25. Rahmim A, Qi J, Sossi V. Resolution modeling in PET imaging: theory, practice, benefits, and pitfalls. *Med Phys.* 2013;40:064301.
26. Dewaraja YK, Frey EC, Sgouros G, et al. MIRD pamphlet no. 23: quantitative SPECT for patient-specific 3-dimensional dosimetry in internal radionuclide therapy. *J Nucl Med.* 2012;53:1310–1325.
27. Li Z, Fessler JA, Mikell JK, Wilderman SJ, Dewaraja YK. DblurDoseNet: a deep residual learning network for voxel radionuclide dosimetry compensating for single-photon emission computerized tomography imaging resolution. *Med Phys.* 2022;49:1216–1230.
28. Jackson P, Hardcastle N, Dawe N, et al. Deep learning renal segmentation for fully automated radiation dose estimation in unsealed source therapy. *Front Oncol.* 2018;8:215.
29. Daniel AJ, Buchanan CE, Allcock T, et al. Automated renal segmentation in healthy and chronic kidney disease subjects using a convolutional neural network. *Magn Reson Med.* 2021;86:1125–1136.
30. Khan J, Rydèn T, Van Essen M, Svensson J, Bernhardt P. Activity concentration estimation in automated kidney segmentation based on convolution neural network method for ^{177}Lu-SPECT/CT kidney dosimetry. *Radiat Prot Dosimetry.* 2021;195:164–171.
31. Lee MS, Kim JH, Paeng JC, et al. Whole-body voxel-based personalized dosimetry: the multiple voxel S-value approach for heterogeneous media with nonuniform activity distributions. *J Nucl Med.* 2018;59:1133–1139.
32. Wilderman SJ, Roberson PL, Bolch WE, Dewaraja YK. Investigation of effect of variations in bone fraction and red marrow cellularity on bone marrow dosimetry in radio-immunotherapy. *Phys Med Biol.* 2013;58:4717–4731.
33. Staanum PF, Frellsen AF, Olesen ML, et al. Practical kidney dosimetry in peptide receptor radionuclide therapy using [^{177}Lu]Lu-DOTATOC and [^{177}Lu]Lu-DOTATATE with focus on uncertainty estimates. *EJNMMI Phys.* 2021;8:78.
34. Willowson KP, Eslick E, Ryu H, et al. Feasibility and accuracy of single timepoint imaging for renal dosimetry following ^{177}Lu-DOTATATE ('Lutate') therapy. *EJNMMI Phys.* 2018;5:33.
35. Baechler S, Hobbs RF, Prideaux AR, Wahl RL, Sgouros G. Extension of the biological effective dose to the MIRD schema and possible implications in radionuclide therapy dosimetry. *Med Phys.* 2008;35:1123–1134.